McCormick

Northwestern Engineering

CCITT · Center for the Commercialization of Innovative Transportation Technologies

Intelligent Structural Health Monitoring of Vehicular Bridges

Using Fiber Optic Sensors to Detect Acoustic Emission

January, 28, 2011

Yan Zhu

Yinian Zhu

Brad Regez

Oluwaseyi Balogun (co-PI)

Sridhar Krishnaswamy (PI)

Disclaimer

The contents of this report reflect the views of the authors, who are responsible for the facts and the accuracy of the information presented herein. This document is disseminated under the sponsorship of the Department of Transportation University Transportation Centers Program, in the interest of information exchange. The U.S. Government assumes no liability for the contents or use thereof..

Preface/ Acknowledgements

This work was funded by the Center for the Commercialization of Innovative Transportation Technology at Northwestern University, a University Transportation Center Program of the Research and Innovative Technology Administration of USDOT through support from the Safe, Accountable, Flexible, Efficient Transportation Equity Act (SAFETEA-LU).

Table of Contents

Notice i
Preface/ Acknowledgements ii
Table of Contents 1
Executive Summary 3
Chapter 1 Fiber Bragg Gratings in Accoustic Emission Monitoring…… ……4
Acoustic Emissions 4
Fiber Bragg Grating Sensors 5
Multiplexing Two-Wave Mixing Interferometer 6
Chapter 2 TWM Interferometric Demodulator Prototype Design……8
Chapter 3 Prototype Testing..... 11
Carbon Fiber Reinforced Polymer (CFRP) Stay Cable 11
Impact and Forced Response of a CFRP Stay Cable 13
Response of a Test Cable Under Cyclic Loading 16
Coupon-Size CFRP / GFRP Samples……18
Verification of FBG strain transfer chirping 18
Tab Design..... 20
Acoustic Emission in the Tab..... 20
Acoustic Emission in the Coupon Samples..... 21
Chapter 4 Conclusions 24
References…….. 25
APPENDIX A. List of Acronyms 27

List of Tables

Table 3-1. Wavelet Transformation 14
Table 3-2. CFRP/GFRP samples and system specifications ……18

List of Figures

Figure 1-1. FBG Schematic 5
Figure 1-2. Multiplexing TWM Interferometer 6
Figure 1-3. Behaivior inside the PRC 7

Figure 2-1. Schematic of the TWM optical table setup 10
Figure 2-2. Compact design of the TWM mixing interferometer 10
Figure 2-3. Plot of temperature vs. resistance reading 11
Figure 2-4 Completed prototype in a aluminum chassis 11

Figure 3-1. CFRP test cable eperiment 9
Figure 3-2. Mounting positions of FBG sensors on cable 10
Figure 3-3. Images of cable failure locations 10
Figure 3-4. Resonant modes of the test cable 11
Figure 3-5. Failed cable time response signal 12
Figure 3-6. Typical cable time response signal 12
Figure 3-7. Wavelet transform between 100-300 kHz 13
Figure 3-8. Wavelet transform greater than 300 kHz 13
Figure 3-9. Cyclic loaded cable response 14
Figure 3-10. Stress vs. strain curves for CFRP and GFRP 19
Figure 3-11. Time history for specimen #3 19
Figure 3-12. Experimental setup for tensile testing 20
Figure 3-13. AE signals observed in FBG sensors 21
Figure 3-14 Time history of specimen #7 22
Figure 3-15. Time response of FBG (1555nm) 22
Figure 3-16. Time response of FBG (1560nm) 23

Executive Summary

The recent collapse of the I-35W Mississippi River Bridge in Minneapolis has spawned a growing interest in the development of reliable techniques for evaluating the structural integrity of civil infrastructure. Current inspection techniques tailored to vehicular bridges in particular are widely based on short-term or intermittent monitoring schedules. While these techniques have had reasonable success in assessing the structural integrity of bridges, there are unanswered questions about their effectiveness for monitoring sudden adverse structural changes that can lead to catastrophic bridge failure. Structural health monitoring (SHM) is an alternative inspection paradigm that provides the potential for long-term monitoring of integrity of large-scale structures.

The goal of this work is to develop an intelligent structural health monitoring (ISHM) scheme for the long-term assessment of the damage state of in-service vehicular bridges. The presented ISHM scheme builds upon an existing SHM scheme developed at the Center for Quality Engineering and Failure Prevention (CQEFP) at Northwestern University for the evaluation of the structural integrity of safety critical infrastructures. The ISHM scheme consists of diagnostic optical fiber Bragg grating (FBG) sensors for acoustic emission monitoring, signal processing techniques for source localization of acoustic emission events, and model based prediction of structural damage using the measured sensor information. Acoustic emissions consist of dynamic elastic stress waves produced by the sudden release of mechanical energy in a material, and their generation is well correlated with the growth of cracks in a structure produced by stress corrosion or mechanical fatigue from cyclic loading. As such, acoustic emission events serve as warning signs for the initiation of the process of structural failure.

CHAPTER 1 – FIBER BRAGG GRATINGS IN ACOUSTIC EMISSION MONITORING

The catastrophic collapse of the Interstate 35W Mississippi River Bridge, also known as Bridge 9340, in 2007 brought nationwide attention to the current condition of U.S. highway infrastructure. Bridge 9340 had been inspected annually since 1993 by the Minnesota DOT and numerous reports were written indicating its structural deficiency. Although warnings had been given and remedial actions were planned, nothing predicted its untimely failure. The investigation led by the National Transportation Safety Board (NTSB) attributed the failure of bridge 9340 to a combination of under designed gusset plates, excessive loading from construction equipment on the bridge, and inefficient corrosion control [1].

In a December 2008 U.S. Department of Transportation (DOT) report, it is stated that of all accounted highway bridges in the US, 25% (151,000) of them are structurally deficient or functionally obsolete. Given past occurrences, current schdedule based inspections alone are not 100% effective in determining the condition of aging structures. The addition of a real-time intelligent structural health management (ISHM) system to a structure can significantly increase safety margins by keeping the owner informed as to the structures current health state.

Acoustic Emission

Acoustic emission (AE) sensors were used in this work for local monitoring of damage evolution in vehicular bridges. AE based inspection techniques have widespread application in the monitoring of cracks and defects in structural materials [2-5]. Acoustic emissions are transient elastic stress waves produced by the sudden release of mechanical energy due to the growth and propagation of cracks in a structure, and are associated with mechanical fatigue loading or stress corrosion. Ultimately, the crack weakens the structure, thus providing a pathway for failure initiation as crack growth persists.

Current AE monitoring systems use piezoelectric sensors to “listen” to the structure. These sensors are costly as each of them requires a preamplifier. The sensors are highly susceptible to electromagnetic interference, have a limited operating frequency range, and require periodic calibration as aging causes a decrease in sensitivity.

The AE system developed in this work utilizes optical fiber Bragg gratings (FBG) in place of piezoelectric sensors. FBG sensors offer numerous advantages compared to piezoelectric sensors for AE monitoring. FBG sensors are low cost and readily available, light-weight, immune to electromagnetic noise sources, and are readily multiplexable. It is possible to set up a FBG array at great distances from the control box with minimal signal loss because the FBG are connected to the control box by fiber optic and not a cable. Having a significantly smaller footprint than the piezoelectric sensors, the FBG can also be mounted in areas with small tolerances. Since they are small, the FBG can be installed permanently to the structure and its fiber runs to each sensor can be concealed easily. This will allow for the inspector to leave the sensor in place to do real-time structural health

monitoring (SHM) of the structure or to leave the sensors in place and simply hook up the demodulator box when a scheduled inspection is required. With this sensing approach, inspectors are not required to set up local sensors, apply coupling fluids for ultrasound transmission, and recalibrate the sensors prior to each use, all of which are necessary for the commonly used piezoelectric SHM sensors. Furthermore, FBG sensors exhibit long-term stability and optical sensitivity, which is suitable for SHM applications.

Fiber Bragg Grating Sensors

FBGs are excellent sensors for detecting AE, and are particularly well suited for long-term SHM applications in safety critical infrastructures [6-8]. The FBG sensor response to an AE event is spectrally encoded in the optical probe, thus providing immunity to noise sources from optical intensity fluctuation and electromagnetic interference. The gauge length of these sensors is small, and multiple sensor elements can be serially multiplexed in a single optical fiber for localized multi-point AE detection without incurring the burden of running massive optical fiber leads through a structure. The sensor can be surface mounted or embedded in a structure, providing a versatile inspection tool. Furthermore, the transmission and reception of optical signals through the sensors can be made over kilometer range distances, thus making FBGs ideal candidates for SHM of large-scale structures.

A fiber Bragg grating in its simplest form consists of an optical fiber with a periodic modulation of the index of refraction in the gauge section of the fiber core as illustrated in figure 1-1, and acts as a wavelength selective mirror based on the Bragg grating resonance condition. In practice, an FBG sensor is interrogated by directing a broadband laser source through the optical fiber. A portion of the input light within a narrow spectral bandwidth is reflected by the Bragg grating, while the remainder of

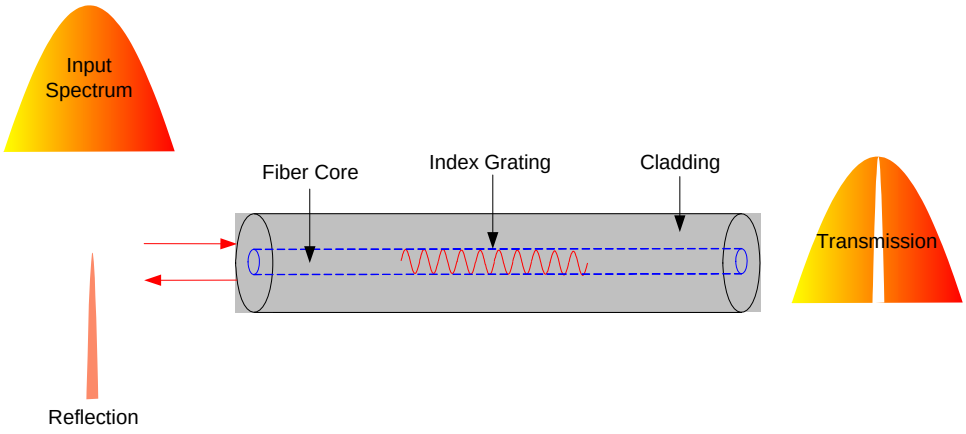

Figure 1-1. A schematic illustration of an optical fiber Bragg grating sensor

the light spectra is transmitted through the optical fiber. The center wavelength λ_0 of the reflected light depends on the effective index of refraction (n_{eff}) of the fiber core, and the period (Λ) of the index of refraction grating in the gauge section, according to the Bragg resonance condition:

$$\lambda_0 = 2n_{eff}.\Lambda \qquad (1)$$

A FBG sensor responds to mechanical or thermal strains imposed by the environment, by a modulation in the phase of the light. Specifically, the center wavelength of the FBG changes as n_{eff} and Λ are perturbed by the imposed external strain. The functional relationship of the FBG spectral shift to these parameters is:

$$\frac{\Delta\lambda_0}{\lambda_0} = \left(1 - \frac{{n_{eff}}^2}{2} p_{12}\right)\varepsilon_1 - \frac{{n_{eff}}^2}{2}\left(p_{11}\varepsilon_2 + p_{12}\varepsilon_3\right) + \beta_0 \Delta T \qquad (2)$$

In the above relationship, $\Delta\lambda_0$ is the spectral shift, ε_1 is the axial strain, ε_2 and ε_3 are the strains in the transverse cross-sectional plane of the core of the optical fiber, the parameters p_{11} and p_{12} are the photoelastic constants, and β_0 is the sum of the coefficient of thermal expansion and the thermo-optic coefficient of the optical fiber. Since measurand in FBG sensor is primarily an optical phase change, a demodulator unit is typically used to convert the phase change to an intensity (or amplitude) change that can be monitored with an optical detector.

Multiplexing Two-Wave Mixing Interferometer

The PI's group at NU has developed a two wave mixing (TWM) interferometer that allows for wavelength demodulation of FBG sensor responses in an InP photorefractive crystal (PRC) [9,10]. The TWM wavelength demodulation scheme offers superior performance characteristics compared to the currently available techniques. The demodulation system is self-adaptive, allowing for selective monitoring of high frequency acoustic emissions over large background signal excursions due to quasi-static temperature drift and low frequency structural deformation. Furthermore, the system allows for multiplexed demodulation of several FBG sensor responses. The mechanical strain sensitivity of the system is remarkably high and dynamic strain amplitudes as low as 0.25 με can be easily recorded. A schematic representing this system is displayed in figure 1-2.

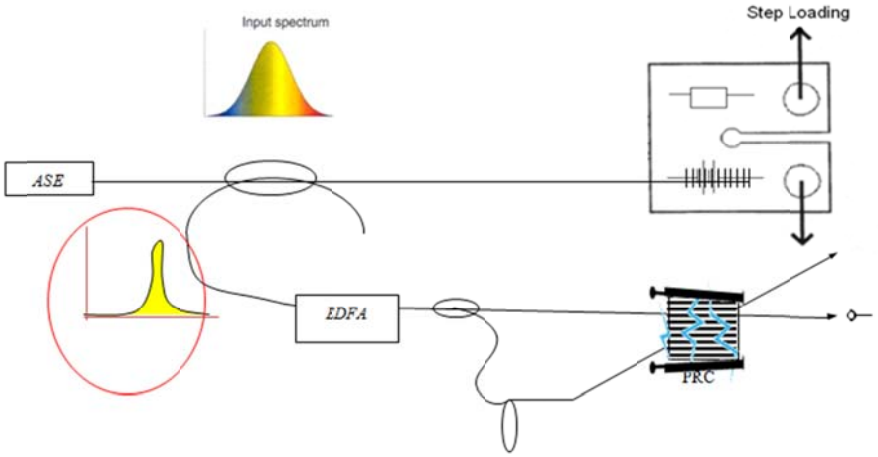

Figure 1-2. Multiplexing Two Wave Mixing interferometer system used to perform high frequency spectral demodulation of FBG sensors

A broadband laser source sends laser light through the FBG sensor. In the diagram, the sensor is mounted on the surface of a test coupon designed for simulated AE monitoring in the PI's laboratory. AE events are generated at the tip of the artificial notch fabricated in the specimen. Light from a broadband amplified spontaneous emission (ASE) source with wavelengths covering the range of 1530 – 1570 nm, is directed to the FBG sensor through an optical circulator. The FBG sensor, acting as a wavelength selective mirror, reflects a portion of the light at its center wavelength. The reflected light is amplified to a peak power of 500 mW in an Erbium doped amplifier. The amplified light is then delivered into the TWM interferometer. In the interferometer, the amplified light is split into signal and

reference beams, with a 5:95 intensity ratio. The signal beam travels directly through the crystal while the pump beam is directed into the crystal with a 6^{o} angle with respect to the signal beam. The two beams interfere inside the crystal creating an optical diffraction grating through the photorefractive effect. A 3kV DC electric field is applied across the side faces of the PRC to enhance the formation of the diffraction gratings. The grating allows for diffraction of the signal and pump beams, such that in the direction of the zero order diffracted signal beam, a diffracted pump beam with a matching wavefront is produced leading to optimal interference of the two beams, which leads to a change in optical intensity as desired. This process is illustrated in Fig. 1.3. In cases, where multiple FBG sensor outputs are directed to the PRC, a corresponding number of diffraction gratings are produced provided that the center wavelengths of the reflecting FBGs are distinctly separated. Each diffraction grating diffracts the signal and pump beams at their corresponding wavelengths, and are separated outside the PRC by directing the exiting light through appropriate band-drop filters. In this work, the minimum FBG wavelength separation needed for multiplexed demodulation in the PRC interferometer is 4 nm. As such, the PRC interferometer can demodulate up to ten FBG sensors simultaneously within the spectral bandwidth of the ASE source.

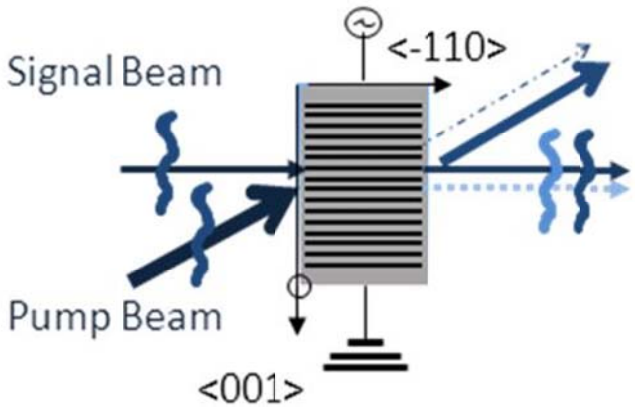

Figure 1-3. Optical Beam Diffraction in a Photorefractive Crystal

A critical component of the demodulation system needs further explaination. One might notice that the wavelength of the signal and pump beams used for sensing originate from the same sensor, both experiencing the same wavelength shift due to an external stimuli. The light beams are made to travel along unmatched optical paths before entering the PRC, which produces a phase shift between the light beams that is related to the sensor response by,

$$\phi(t) = -\frac{2\pi d}{\lambda^2}\Delta\lambda \tag{6}$$

where d is the optical path length difference (OPD), λ is the nominal center wavelength of the light from FBG sensor, $\Delta\lambda$ is the time-varying shift in the wavelength caused by the external stimuli. The phase shift described by Eq. (6) is demodulated as an intensity change through the interference of the transmitted signal and diffracted light beams exiting the PRC.

Another important characteristic of the demodulator is its response time. The photorefractive diffraction gratings are produced in the PRC within a finite time τ. When changes in $\phi(t)$ occur on a slow time scale that is smaller than t, the diffraction gratings are erased and a new one is formed. As

such, the system can be thought of as losing memory of the slow changes in sensor wavelength $\Delta\lambda$. Consequently, the PRC interferometer allows for dynamic sensor wavelength changes to be selectively demodulated in the presence of low frequency sensor responses arising from heating effects or large quasi-static deformation. The response time of the PRC demodulator is 1 ms, and sensor responses in the range of 1 kHz and above can be readily demodulated. The upper threshold on the frequency response is limited by the bandwidth of the optical detector and coupling electronics. At the moment, the limit is in the range of 10 MHz.

CHAPTER 2- TWO-WAVE MIXING (TWM) INTERFEROMETRIC DEMODULATOR PROTOTYPE DESIGN

The compact and adaptive interferometric wavelength demodulator is designed and assembled using compact microbench components and free space optical components. The demodulator has the ability to compensate for quasi-static drifts without the need for active stabilization. It is suitable for measuring dynamic and transient strain from impact events, vibration, and acoustic emissions. It can also be functionalized with wavelength division multiplexing for multi-channel detection. A schematic of TWM is illustrated in figure 2-1, with an optical table design (a) of the TWM and a portable design (b) with the mounting of the crystal expanded above. The high voltage electric field is applied to the PRC using the two elecrrodes mounted on opposite sides of the holding fixture. This optical setup is integrated into a small format consisting of 4 tiers: optics, power supply and electronics, a level for each of the EDFAs, with the optics level shown in figure 2-2 (a) with the optical level shown in (b). A semiconducting thermistor is used in temperature monitoring for photorefractive crystal and exhibits a nonlinear behavior in its conversion from resistance to temperature, which is plotted in figure 2-3 (a). It is selected in order to avoid electrical conductance when reading the themistor output when a high voltage field is applied across the crystal. To linearize the behavior of the semiconductor, an electrical circuit figure 2-3 is designed to analogically represent Steinhart-Hart equation:

$$T = \left[A + B\ln(R) + C(\ln(R))^3\right]^{-1} \quad (14)$$

where A, B, and C are the Steinhart-Hart coefficients, depending upon the type and model of the thermistor and driving current used and the temperature range of interest. R is the resistance at specified temperature in ohms. T is the temperature in Kelvin. Converting thermistor resistance to a temperature value is necessary to develop a PID controlled temperature controller. Figure 2-1 (b) illustrates that the thermistor is used to determine the temperature in the crystal. Using the analog circuit, resistance in the thermistor is converted to temperature, which is then compared to the set temperature. A summing amplifier is used to determine the difference between the set temperature and the thermistor output. Then, using a PID controller, TEC current output is adjusted to maintain the crystal temperature at the set temperature. The whole system is packaged in a robust (22”x17”x9”) aluminum chassis that can be rack mounted (figure 2-4).

(a)

Figure 2-1. Schematic of the optical table setup of a two-wave mixing interferometer (a) [37] and its portable design (b) with the crystal mount illustrated above.

(a))

Figure 2-2. A compact design of the two-wave mixing interferometer demodulation system comprises of optical stage, power sector, and two levels of EDFAs (a) with the optical stage shown in (b).

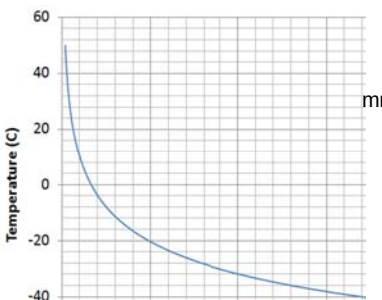

mmercialization c f In

Int elli

(a))

Figure 2-3. (a) plot of temperature vs. resistance reading for TCS10K5 semiconductor thermistor and (b) electrical representation of Steinhart-Hart equation used to convert resistance to temperature for semiconducting thermistor.

Figure 2-4. Completed prototype in a aluminum chassis

CHAPTER 3- PROTOTYPE TESTING

Carbon Fiber Reinforced Plastic (CFRP) Stay Cable

The performance of a CFRP stay cable is investigated under varying loading conditions. The cable consists of 7 CFRP strands of 7 mm diameter and is covered with polyethylene (PE) sheaths, shown in figure 3-1 (b). The 1.6 m test cable has a gauge length of 0.8 m with two grip lengths of 0.4 m. The tensile strength, elastic modulus, and ultimate strain of the CFRP wire are 2200MPa, 200GPa, and 2.42%, respectively [12]. The cable anchorages are held on each end by the grips of the load frame as illustrated in figure 3-1 (a). The test ran on a single cable for a total of 3.9 hrs over the span of 3 days.

(a)

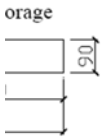

b)

Figure 3-1. Experimental conditions for the CFRP test cable: (a) the test cable is mounted on the MTS machine as illustrated above. (b) The test cable consists of 7 (dia. 7 mm) CFRP wires bounded by PE sheath.

The demodulator is employed to perform vibration and acoustic emission monitoring in the CFRP stay cable under various loading conditions. Two FBG mounting locations are used during the test, displayed in figure 3-2 (a) and (b). During the middle of the last set of testing, FBG sensor #1 was strained to failure and the test is continued monitoring FBG sensor #2 until the CFRP cable failed. After the test cable is fatigued for 19504 cycles, no significant damage is observed either by appearance or by using the demodulator. The test cable is then stretched until failure by displacing the top grip by 0.05 mm/s (see figure 3-3 (a)). Upon total failure, the test cable region near the bottom

grip shown in figure 3-3(b) failed first and total failure occurred when the region near the top grip gave out, indicated by the audible and visible fiber breakages, shown in figure 3-3(c).

(a) (b)

Figure 3-2. Mounting positions of FBG sensors: (a) FBG sensor #1 is mounted on the CFRP wire, where most of the data is collected and (b) FBG sensor #2, mounted on the anchorage, is employed after sensor #1 failed.

(a) (b) (c)

Figure 3-3. Pictures of test cable failure locations: (a) test cable failed in two locations near the top grip and (b) near the bottom grip as well as (c) total cable failure illustrated by fiber breakage.

Impact and Forced Response of a CFRP stay cable

The test cable is bounded on both ends and elongated by 4 mm and then is excited by impulse tapping. The dynamic mechanical strain produced by transient impulse excitation and the resonant modes under fixed-fixed boundary condition are obtained using FBG sensor/spectral demodulation system. Figure 3-4(a) illustrates the transient mechanical strains measured by the FBG sensor and

figure 3-4 (b) shows the amplitude spectrum of the fast Fourier transform (FFT) of the measured data. The amplitude spectrum shows four dominant resonant modes below 200 Hz: at 0.5 Hz, 90.5 Hz, 97.5 Hz, and 179.7 Hz.

(a) (b)

Figure 3-4. Resonant modes of the test cable under fixed-fixed boundary condition: (a) time history of the impulse excitation and (b) FFT of the measured data.

Figure 3-5(a) is measured data obtained from FBG sensor #1 during the last session of the experimental testing, in which the test cable is stretched until failure. Although it is suspected that the spectrum of the FBG profile has been damage, measured data is still obtained. Comparing figure 3-4(b) and figure 3-5(b), resonant peaks in figure 3-5(b), where forced excitation is applied the test cable, are much more distinctive. Also, note the slight increase in frequency in the fourth resonant mode from 179.7 Hz to 181 Hz. The inaccuracy in low-frequency modal analysis could be attributed to chirped FBG.

Due to the large amount of data, portions of the time history in figure 3-5 (a) are selected to perform analysis, shown in figure 3-6 (a). The black, red, and blue lines in figure 3-6(a) display multiple cycles, two cycles, and one cycle of the time history, respectively. FFT is performed on each of the selected data, with some distinct peaks highlighted in figure 3-6(b). De Groot *et al.* [13] correlated the specific acoustic emission frequency range with defined failure modes such as matrix cracking, debonding, fiber pull-out, and fiber failure. The authors determined that matrix-cracking released frequencies are of order of 100 kHz and frequencies generated by fibers are above 300 kHz. Debonding frequencies and pull-out frequencies are interchangeable, from 180 to 310 kHz. The one cycle of the time history in figure 3-6 (a) is filtered to observe the frequency contents between 100 kHz to 300 kHz, illustrated in figure 3-7. From the figure, it can be seen that the AEs in this frequency range is continuous, possibly due to matrix damage. Figure 3-8 shows the frequency filter (>300kHz) applied to one cycle time history in Figure 3-6 (a). The distinctive burst cycles could indicate fiber damage. The two wavelet analyses are overlapped to illustrate the simultaneous occurrences of matrix and fiber damages.

(a) (b)

Figure 3-5. Response obtained when the test cable is strained until failure: (a) time history and (b) FFT of the measured data.

Figure 3-6. (a) Selected time response from time history in figure above. (b) FFT for measured data with selected frequency peaks shown.

Similar conclusions are made by the results collected from research performed by Li [12]. In this research effort, 8 FRP cables are fatigued, of which 5 were made of carbon. Using PZT based AE sensors, AE signals generated by the damage of cables are recorded. Each of the cables exhibited different frequencies spectra. However, it can be generalized that the frequency range located between 0.5 to 250 kHz can be attributed to mostly matrix damage and frequencies of 340 kHz to 500 kHz correspond to fiber failure. High concentrations of energy above 250 kHz could indicate complex interaction of matrix cracking, fiber-matrix splitter and fiber fracture as it is concluded by de Groot [13].

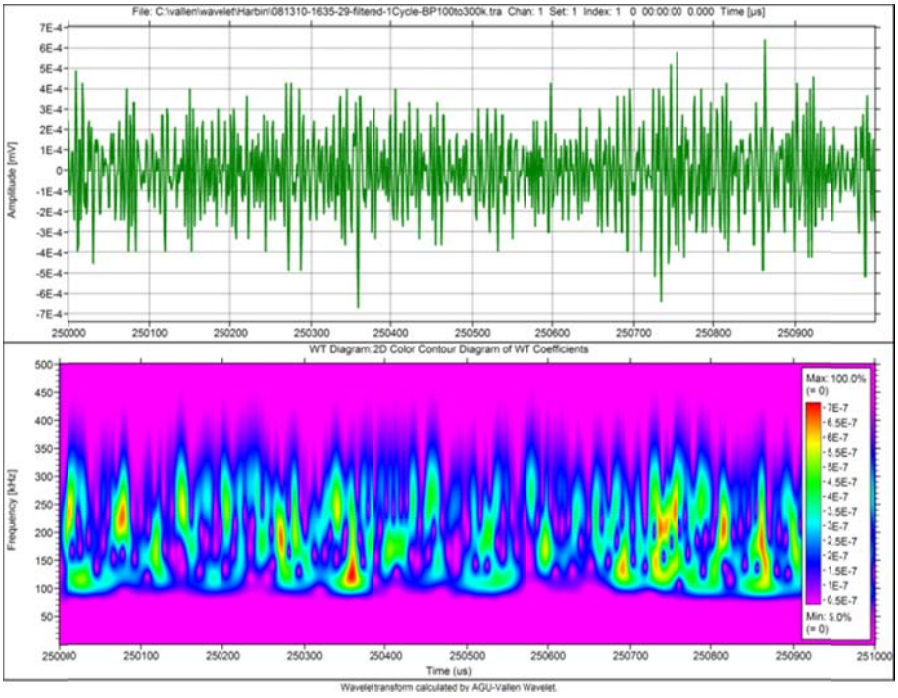

Figure 3-7. Wavelet transform of Figure 20(a) with frequency contents between 100kHz to 300kHz.

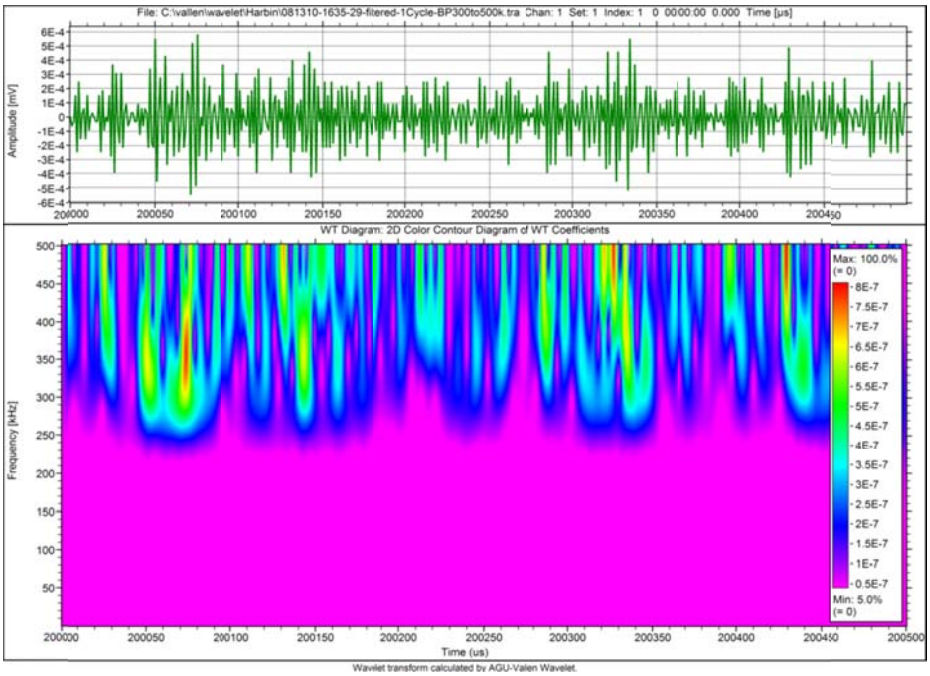

Figure 3-8. Wavelet transform of Figure 20(a) with frequency contents above 300kHz.

Response of a test cable under cyclic loading

The test cable is fixed on both ends where the top grip is moved at the frequency and number of cycles indicated in table 3-1. Figure 3-9(a) and figure 3-9(b) displays the FBG response when the test cable is cycled at 1 Hz with a deformation of 0.6875% and 2 Hz with a deformation of 0.8125%, respectively. As indicated in table 3-1, 0.6875% strain is equivalent to a shift of 8.25 nm in wavelength, whereas 0.8125% equates to 9.75 nm wavelength shift using

$$1\ \mu\varepsilon = 1.2\ \text{pm} \tag{14}$$

Throughout this experimental investigation, it is observed that the large amplitude low-frequency mechanical strain greatly dominated, making it difficult to detect high frequency emission from structural damage. The large deformation on the testing cable is transferred to the FBG, damaging the FBG spectral profile.

Table 3-1. Wavelet transform of Figure 20(a) with frequency contents above 300kHz.

Time History	Running Time (s)	Cycle	Freq (Hz)	% of Strain	Wavelength Shift (nm)
8/11/2010 14:06	2444	2683	1	0.6875	8.25
8/11/2010 15:01	600	60	0.1	0.6875	8.25
8/12/2010 11:15	5017	5016	1	0.8125	9.75
8/12/2010 12:42	3681	7361	2	0.875	10.5
8/12/2010 16:37	189	377	2	0.8125	9.75
8/13/2010 15:38	1002	2003	2	0.875	10.5
8/13/2010 16:00	668	2004	3	1.0625	12.75
8/13/2010 16:33	513	Undergo tension at 0.05mm/s until failure			
Total:	14114	19504			

Figure 3-9. Response obtained when test cable is cyclic loaded: (a) 1Hz and (b) 2Hz

Coupon-Size Carbon Fiber Reinforced Polymer (CFRP)/GFRP Samples

To further investigate the behaivior of the CFRP cable during the tensile testing, FBGs are mounted on coupon-sized CFRP/GFRP samples and subjected to tensile loading. A total of 8 specimens are tested, of which 3 are carbon-based (Tyfo® SCH-41 Composite) and 5 are glass based (Tyfo® SEH-51 Composite). Stress vs. strain curves for two types of specimens used are given in Figure **3-10** (a) and (b), respectively.

Verification of FBG chirping behavior due to strain transfer

Specimen 1, 2, 4, and 5 are tested without any sensors and used to observe the failure behavior in these composite samples. Figure 3-11 displays the testing time history of specimen #3, where the upper left corner displays the location of the FBG sensor and the boxed figures illustrates acoustic emissions detected during the course of the experiment. During the tensile testing of specimen #3, the experiment is paused 3 times, during which the FBG profile is inspected using a tunable laser. After 0.9% strain, chirping behavior is concluded to have occurred in the FBG profile, when a single wavelength is not detected using the tunable laser source. Because the Michelson interferometer can detect only one wavelength interference, demodulation is still possible. Therefore, acoustic emission is detected subsquent to FBG chirping. In order to demodulate multiple FBG sensors simultaneously, it is imperative that the reflective profile of the FBG must remain narrow and only one frequency is reflected. Thus, a new experimental testing scheme is developed, as shown in Figure 28.

Table 3-2. CFRP/GFRP coupon-size samples and system specifications.

Specimen #	Gage Length (m)	Material	# of FBGs	FBG Mounting Loc.	Demodulation Schemes
1	0.223	GFRP	-	-	-
2	0.235	GFRP	-	-	-
3	0.22	GFRP	1	Coupon	MI
4	0.226	CFRP	-	-	-
5	0.21	CFRP	-	-	-
6	0.218	CFRP	1	Coupon	MI
7	0.206	GFRP	2	Tabs	TWMI
8	0.209	GFRP	1	Tabs	TWMI

Figure 3-10. Stress vs. strain curves for: (a) CFRP and (b) GFRP.

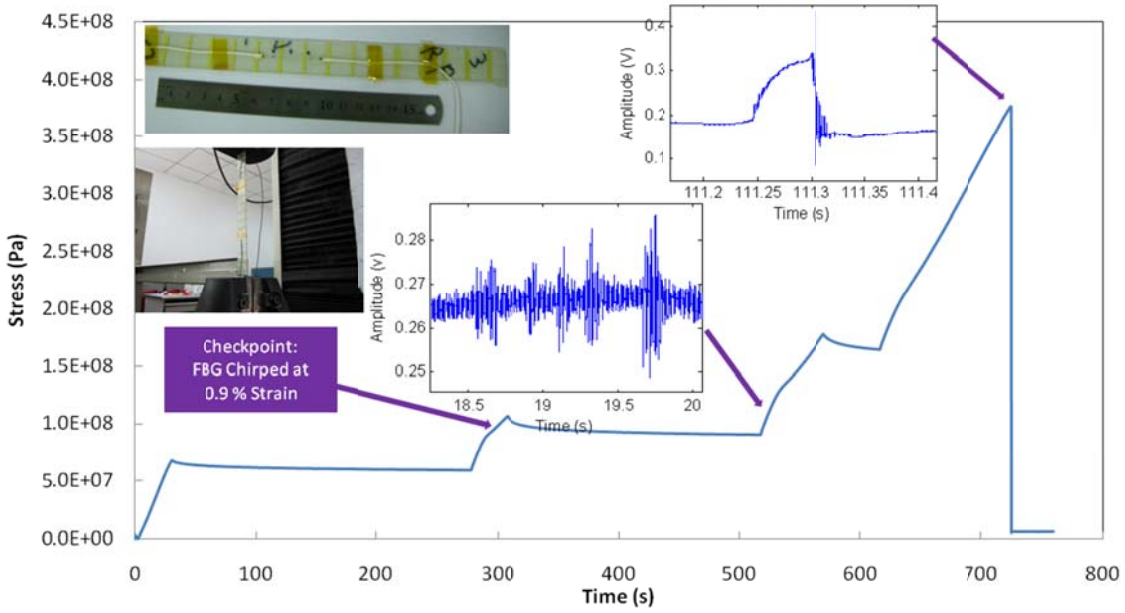

Figure 3-11. Time history for specimen #3 (see Error! Reference source not found.**).**

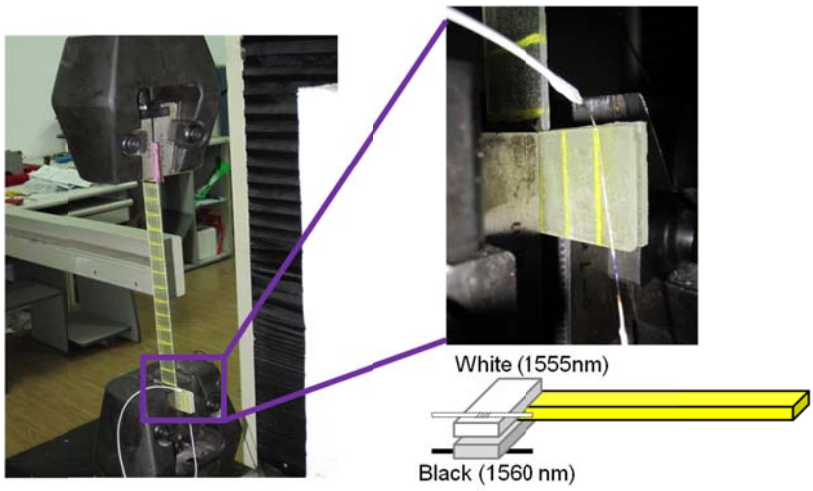

Figure 3-12. (a) Experimental setup for tensile testing on coupon size samples and (b) close-up on the tab design.

Tab Design

The purpose of this tab design is to mitigate the large strain on the FBG sensors when the specimen is subjected to loading, by having the tab act as a wave-guide and couple the stress wave into the FBG sensors. Figure 3-12(a) shows the testing frame and the use of sandpaper to enhance the grip on the specimen. Figure 3-12(b) illustrates the tab design, where the specimen is sandwiched in between two tabs made of the same material as the specimen. An FBG sensor is mounted on the cantilever end of each of the tabs. Since two FBG sensors are used in this case, TWMI is used to perform the demodulation.

Acoustic Emission in the Tab

Measurement data shown in Figure 3-13 is collected prior to loading the specimen. The acoustic emission collected in this case is caused by sandpaper being pressed into the tabs as the loading frame adjusts its grip on the specimen. Two types of acoustic emission signals are observed: continuous and burst. Large amount of continuous AE signal indicates matrix failure whereas the discrete burst AE signal could point to fiber failure. Figure 3-13(a) shows the measured time domain data and the corresponding wavelet transform for continuous AE signals. The wavelet data shows high mechanical strain energy concentrated at 35 kHz. Figure 3-13(b) illustrates transformed data with mechanical strain energy extending up to 125 kHz for burst AE signal. Although both types of AE signal exhibits ultrasonic energy up to 100 kHz, most of the energy resulting from matrix failure is concentrated around 35 kHz, and the amplitude of energy released due to matrix failure is much smaller than the energy released due to fiber failure. Because the damage induced by the sandpaper is on the tab, low amplitude ultrasonic energy released due to matrix failure is able to be detected.

Acoustic Emission in the Coupon Samples

During tensile testing of the specimen, only two incidents of acoustic emissions are detected. Figure 3-14 illustrates the time history of specimen #7 under tensile loading. The small amount of energy released from matrix failure in the specimen could be not efficiently be coupled through the tab, resulting in lack of continuous AE detection. Only burst AEs are observed in the data. Toward the end of the specimen #7 time history, 4 distinct burst AEs are detected. By applying wavelet transform to each individual burst, it is observed that energy released is concentrated and is different from one tab from the other. Figure 3-15(a) is time history data and (b) is the transformed data of the burst time signal for FBG 1555nm with concentrated ultrasonic energy at 15.07 kHz. Figure 3-16(a) displays the time history and (b) illustrates the transformed result for FBG 1560nm with ultrasonic energy focused at 11.9 kHz. The ultrasonic energy at these repeated frequencies corresponds to a specific FBG led to the conclusion that the tabs are acting as cantilever resonators rather than waveguides. Energy occurred during the release of emission events drives the tabs to resonate at those frequencies, which is then detected by the FBG sensors.

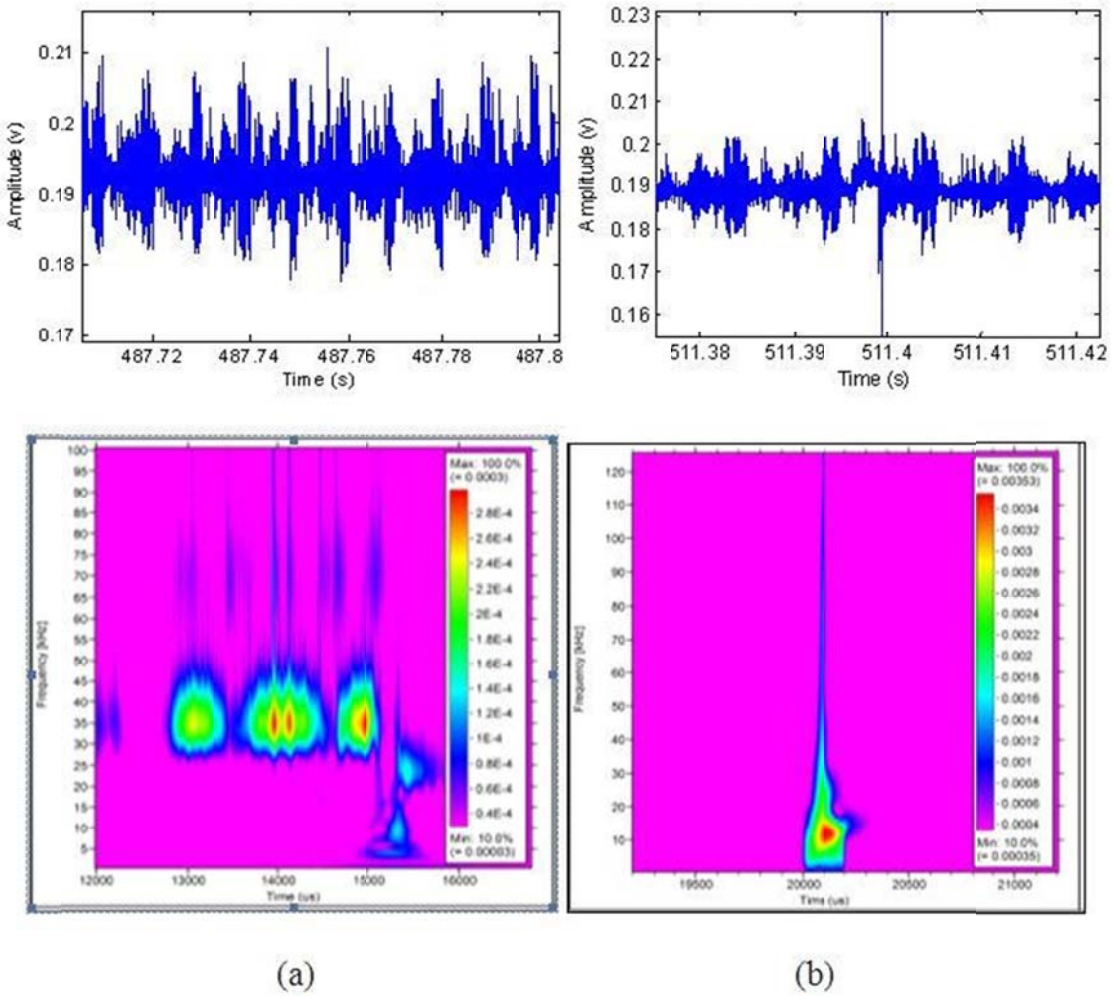

Figure 3-13. Acoustic emission signals (top) observed in FBG sensors and the corresponding wavelets transform (bottom): (a) continuous and (b) burst.

Figure 3-14. Time history of specimen #7.

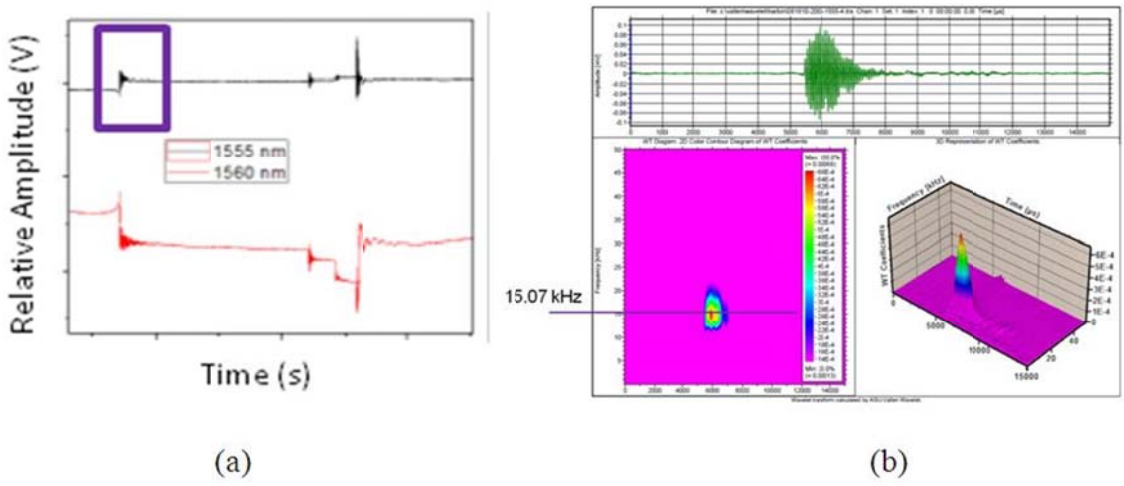

Figure 3-15. (a) Time response of FBG (1555nm) and (b) Wavelet transform of measured data in purple.

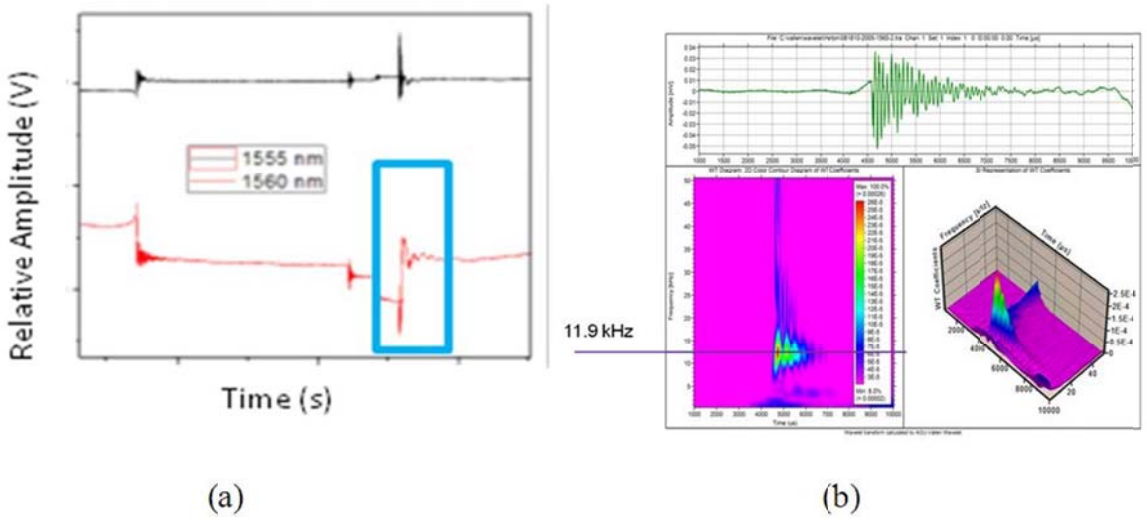

Figure 3-16. (a) Time response of FBG (1560nm) and (b) Wavelet transform of measured data in blue.

CHAPTER 4- CONCLUSION

The objectives of this project are to develop a rugged construction of the two-wave mixing FBG demodulation system developed by the PI's group, and to conduct pilot field tests on acoustic emission diagnostics of local damage in vehicular bridge components using FBG sensors. This project is motivated by the unique capabilities provided by the demodulation system, namely, low cost demodulation approach, multiplexed demodulation of multiple sensor responses, adaptivity to low frequency noise from thermal drifts and large quasi-static deformation, high mechanical strain amplitude sensivity, and high frequency (~ a few hundred kilohertz) response of the demodulator. Prior to the commencement of this project, a basic proof of concept of the demodulation scheme was demonstrated by the PI on a laboratory breadboard. The system described in this report was fabricated in a compact form using microbench components and a free space optics currently housed in a rack mounted enclosure that is suitable for field testing applications. A set of pilot field tests were conducted in collaboration with research partners at the Hong Kong Polytechnic University in Hong Kong, and the Dalian University of Technology in China. These tests involved the monitoring of crack initiation and propagation in the carbon fiber reinforced composite test coupons loaded in uni-axial tension and with cylic loads through to complete specimen fracture. The data allowed for delineation of various instrinsic microstructual damage modes including matrix rubbing and damage in the test coupons. In the case of the unitaxial tension tests, the results obtained from the FBG sensor indicates a clear delineation between the loading regimes of the specimen. Also, the cyclic loading data are well correlated with the loading history of the test coupons. The results obtained demonstrate the high sensitivity of FBG sensors to local damage evolution in component parts. At present, we are investigating potential field testing of local damage in a vehicular bridge at sites within the US.

References

[1] T. N. Williams. (2008, NTSB Acting Chairman Discusses Board's Investigation of I-35W Bridge Collapse at National Conference of State Legislatures. NTSB News

[2] Sison M., Duke J.C. Jr., Lozev G.G., Clemena G.G., “Analysis of Acoustic Emissions from a Steel Bridge Hanger”, Res. Nondestr Eval, 10, 123 – 145, (1998)

[3] Shigeishi M., Colombo S., Broughton K.J., Rutledge H., Batchelor A.J., and Forde M.C., “Acoustic emission to assess and monitor the integrity of bridges”, Construction and Building Materials, 15, 35-49, (2000)

[4] Tennyson R.C., Mufti A.A., Rizkalla S., Tadros G., and Benmokrane B., “Structural health monitoring of innovative bridges in Canada with fiber optic sensors”, Smart Mater. Struct., 10, 560-573, (2001)

[5] Prine D.W., “Application of acoustic emission and strain gauge monitoring to steel highway bridges”, Proc. ASNT 1994 Spring Conf., New Orleans, LA, 90-92, (1994)

[6] Ansari F. (ed.), Fiber Optic Sensors for Construction Materials and Bridges (Technomic Publishing Company, 1998)

[7] Othonis A., “Fiber Bragg Gratings”, Rev. Sci. Instrum., 68(12), 4309-4341, (1997)

[8] Todd M.D., Nichols J.M., Trickey S.T., Seaver M., Nichols C.J., and Virgin L.N., “Bragg grating-based fiber optic sensors in structural health monitoring”, Phil. Trans. R. Soc. A, 365, 317-343, (2007)

[9] Qiao Y., Zhou Y., and Krishnaswamy S., “Adaptive demodulation of dynamic signals from fiber Bragg gratings using two-wave mixing technology”, Appl. Opt. 45(21), 5132-5142, (2006)

[10] Balogun O., Kirikeira G.R., Krishnaswamy S., “Optimal demodulation of wavelength shifts in a fiber Bragg grating sensor using an adaptive two wave mixing photorefractive interferometer”, Sensors and Smart Structures Technologies for Civil, Mechanical and Aerospace Structures 2008, Proc. SPIE., 6932, 69322K, (2008)

[11] Y. Qiao, "Adaptive demodulation of dynamic signals from fiber Bragg grating sensors using two-wave mixing interferometry in indium phosphide:iron," Ph.D. Dissertation, Mechanical Engineering, Northwestern University, Evanston, 2006.

[12] H. Li, Huang, Y.,Chen, W.L., Ma, M.L., Tao, D.W.,& Ou, J.P., "Estimation and Warning of Fatigue Damage of FRP Stay Cables Based on Acoustic Emission Technique and Fractal Theory."

[13] P. J. de Groot, et al., "Real-time frequency determination of acoustic emission for different fracture mechanisms in carbon/epoxy composites," Composites Science and Technology, vol. 55, pp. 405-412, 1995.

List of Acronyms

AE	Acoustic Emissions
CFRP	Carbon Fiber Reinforced Polymer
CQEFP	Center for Quality Engineering and Failure Prevention
DOT	Department of Transportation
EDFA	Erbium Doped Fiber Amplifier
FRP	Fiber Reinforced Plastic
GFRP	Glass Fiber Reinforced Polymer
ISHM	Intelligent Structural Health Managment
PRC	Photorefractive Crystal
SHM	Structural Health Monitoring
TWM	Two Wave Mixing